Cross section measurement of ^{14}N$(p,\gamma)^{15}$O in the CNO cycle

Q. Li,[1,2,*] J. Görres,[1,2] R. J. deBoer,[1,2,†] G. Imbriani,[1,3] A. Best,[1,2,‡] A. Kontos,[1,2,§] P. J. LeBlanc,[1,2] E. Uberseder,[1,2] and M. Wiescher[1,2]

[1]*Department of Physics, University of Notre Dame, Notre Dame, Indiana 46556, USA*

[2]*The Joint Institute for Nuclear Astrophysics, University of Notre Dame, Notre Dame, Indiana 46556, USA*

[3]*Università degli Studi di Napoli "Federico II" and INFN, Napoli, Italy*

(Received 22 January 2016; published 23 May 2016)

Background: The CNO cycle is the main energy source in stars more massive than our sun; it defines the energy production and the cycle time that lead to the lifetime of massive stars, and it is an important tool for the determination of the age of globular clusters. In our sun about 1.6% of the total solar neutrino flux comes from the CNO cycle. The largest uncertainty in the prediction of this CNO flux from the standard solar model comes from the uncertainty in the ^{14}N$(p,\gamma)^{15}$O reaction rate; thus, the determination of the cross section at astrophysical temperatures is of great interest.

Purpose: The total cross section of the ^{14}N$(p,\gamma)^{15}$O reaction has large contributions from the transitions to the $E_x = 6.79$ MeV excited state and the ground state of ^{15}O. The $E_x = 6.79$ MeV transition is dominated by radiative direct capture, while the ground state is a complex mixture of direct and resonance capture components and the interferences between them. Recent studies have concentrated on cross-section measurements at very low energies, but broad resonances at higher energy may also play a role. A single measurement has been made that covers a broad higher-energy range but it has large uncertainties stemming from uncorrected summing effects. Furthermore, the extrapolations of the cross section vary significantly depending on the data sets considered. Thus, new direct measurements have been made to improve the previous high-energy studies and to better constrain the extrapolation.

Methods: Measurements were performed at the low-energy accelerator facilities of the nuclear science laboratory at the University of Notre Dame. The cross section was measured over the proton energy range from $E_p = 0.7$ to 3.6 MeV for both the ground state and the $E_x = 6.79$ MeV transitions at $\theta_{\text{lab}} = 0°, 45°, 90°, 135°$, and 150°. Both TiN and implanted-^{14}N targets were utilized. γ rays were detected by using an array of high-purity germanium detectors.

Results: The excitation function as well as angular distributions of the two transitions were measured. A multichannel R-matrix analysis was performed with the present data and is compared with previous measurements. The analysis covers a wide energy range so that the contributions from broad resonances and direct capture can be better constrained.

Conclusion: The astrophysical S factors of the $E_x = 6.79$ MeV and the ground-state transitions were extrapolated to low energies with the newly measured differential-cross-section data. Based on the present work, the extrapolations yield $S_{6.79}(0) = 1.29 \pm 0.04(\text{stat}) \pm 0.09(\text{syst})$ keV b and $S_{\text{g.s.}}(0) = 0.42 \pm 0.04(\text{stat})$ keV b. While significant improvement and consistency is found in modeling the $E_x = 6.79$ MeV transition, large inconsistencies in both the R-matrix fitting and the low-energy data are reaffirmed for the ground-state transition. Reflecting this, a systematic uncertainty of $^{+0.09}_{-0.19}$ keV b is recommended for the ground-state transition.

DOI: 10.1103/PhysRevC.93.055806

I. INTRODUCTION

During the main-sequence stage, stars generate energy through hydrogen burning: the pp chains and the CNO cycles [1]. In stars more massive than our sun, the density and temperature are high enough for the CNO cycles to dominate the energy production. The main CNO cycle contributes 99% of the total CNO energy production in the Sun [2]. The ^{14}N$(p,\gamma)^{15}$O reaction is the slowest in the main cycle, thus determining the energy production and the timescale of hydrogen consumption. The efficiency by which the CNO cycle converts hydrogen into helium, and therefore its energy-production rate, is directly correlated with the turnoff point from the main sequence of low-mass stars. This can be observed from astronomical data from globular clusters, environments where the ages of many of the stars are similar, by constructing color-magnitude diagrams. Stellar models can be used to calculate the turnoff point and are quite sensitive to the overall rate of the CNO cycle and therefore to the rate of the ^{14}N$(p,\gamma)^{15}$O reaction [3]. In stars like our Sun, the CNO cycles produce about 1% of the total solar energy [4] and contribute about 1.6% of the total solar neutrino flux [5]. Besides the uncertainties in the reaction rates of ^{3}He$(\alpha,\gamma)^{7}$Be and ^{7}Be$(p,\gamma)^{8}$B in the pp chains, the ^{14}N$(p,\gamma)^{15}$O reaction is one of the largest sources of uncertainty in standard-solar-model neutrino-flux predictions [6].

*qli3@nd.edu

†rdeboer1@nd.edu

‡Present address: Università degli Studi di Napoli "Federico II" and INFN, Napoli, Italy.

§Present address: LIGO, Massachusetts Institute of Technology, Cambridge, Massachusetts 02139, USA.

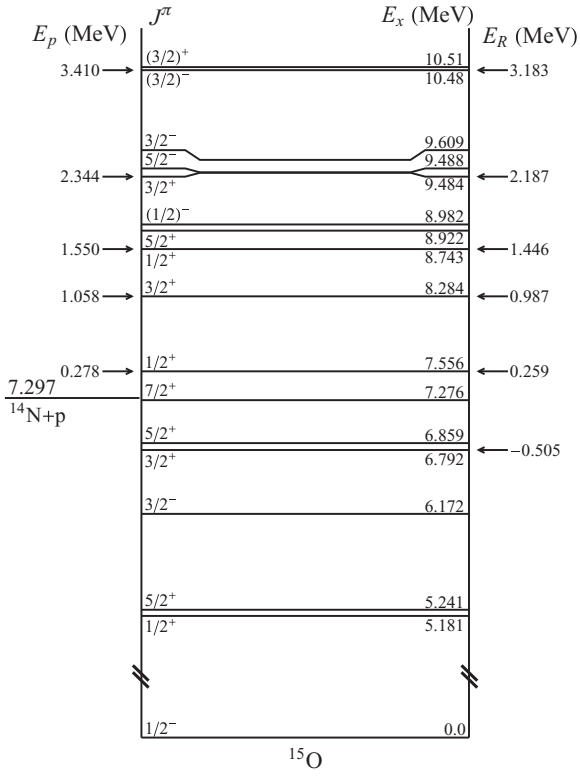

FIG. 1. Level scheme of the ^{15}O compound nucleus. The beam (laboratory frame) and resonance (center-of-mass frame) energies and corresponding excitation energies of the important states are given.

The tabulated reaction rate data (see, e.g., Refs. [3,7,8]) rely on a comprehensive study of the ^{14}N$(p,\gamma)^{15}$O reaction where the only data at $E_{\text{c.m.}} > 0.6$ MeV were those of Schröder *et al.* (1987) [9]. The measurement covered the proton-energy range from $E_p = 0.2$ to 3.6 MeV. Both excitation functions and angular distributions were reported. By fitting interfering Breit–Wigner functions, the total S factor at zero energy $S(0)$ was determined to be 3.20 ± 0.54 keV b with contributions mainly from the transition to the ground state followed by the transition to the $E_x = 6.79$ MeV bound state. The large contribution of the ground-state transition comes primarily from the subthreshold resonance at $E_R = -0.505$ MeV, which corresponds to the $E_x = 6.79$ MeV level in the ^{15}O compound nucleus (Fig. 1). From the fitting of the cross-section data, the width was determined to be $\Gamma_\gamma^{6.79} = 6.3$ eV. The angular distributions of all transitions exhibit a symmetric pattern around 90° except for the ground-state transition, which appears to have a nonzero a_1 term in the angular distribution coefficients.

In an independent R-matrix analysis by Angulo *et al.* (2001) [10], the extrapolated S factor was reduced by a factor of 1.7. The contribution from the subthreshold state was found to be much weaker than what Schröder *et al.* [9] predicted because a smaller value for the width, $\Gamma_\gamma^{6.79} = 1.75$ eV, was obtained.

More recent measurements [11–15] have focused on the cross section around the lowest energy resonance at $E_p =$ 278 keV. The lowest-energy measurement was carried out by the LUNA Collaboration [13,14] down to $E_{\text{c.m.}} = 70$ keV. An R-matrix analysis based on all the available experimental data was recently performed by Azuma *et al.* [16]. As discussed in Refs. [3,4], summing-in corrections were not properly taken into account in the higher-energy measurements of the ground-state-transition data of Ref. [9]. It has been shown [4,11,12,15–17] that including the higher-energy data from Ref. [9] can lead to a different extrapolation than that obtained by fitting only the lower-energy data. Furthermore, it is unclear if the nonzero a_1 contribution in the ground-state transition has an effect on the S-factor extrapolation. Thus new differential-cross-section measurements over the higher-energy region are necessary to provide more robust extrapolations.

In Sec. II the experimental setup and procedures are described. The angle-integrated cross sections are presented and compared with previous data in Sec. III as is an R-matrix analysis that fits the angular distributions directly, and an extrapolation is made to stellar energies. Finally, the results are summarized in Sec. IV.

II. EXPERIMENT PROCEDURES

The experiments were performed by using the 1 MV JN and 4 MV KN Van de Graaff accelerators located at the nuclear science laboratory at the University of Notre Dame. The KN accelerator was used to produced protons over the energy range from $E_p = 0.6$ to 3.6 MeV, while the JN covered the range from $E_p = 0.27$ to 0.8 MeV. Typical proton-beam intensities were between 10 and 40 μA. Both TiN sputtered targets and implanted-^{14}N solid targets were utilized. The natural TiN targets (50 nm) were produced by sputtering a layer of Ti onto a Ta backing in a nitrogen atmosphere. Because the high count rate from the ^{15}N$(p,\alpha_1\gamma)^{12}$C reaction will hinder the measurement of the ^{14}N$(p,\gamma)^{15}$O cross section at higher energy, isotopically pure implanted targets were used. The targets were made at the University of Bochum by implanting ^{14}N ions onto a Ta backing using a 500 kV Cockcroft–Walton accelerator [18]. Several thin targets and one thick target were produced. The energy loss of the protons in the thin targets at the $E_p = 278$ keV resonance was between 8.4 and 14.8 keV with an uncertainty of ∼6%. The thick target corresponded to a proton energy loss of 72.4 ± 5.7 keV. During the low-energy measurements with the JN accelerator, the target profiles of TiN and implanted targets were monitored by repeatedly scanning the $E_p = 278$ keV ($\Gamma_{\text{lab}} = 0.96 \pm 0.05$ keV [3]) resonance of the ^{14}N$(p,\gamma)^{15}$O reaction. For high-energy measurements on the KN accelerator, the $E_p = 1.06$ MeV ($\Gamma_{\text{lab}} = 3.9$ keV [19]) resonance was used to monitor the target profile. For the monitoring, the targets were mounted on a target holder placed at 45° with respect of the beam direction to reduce the angular distribution effects.

Two setups were employed as shown in Fig. 2. For the angular distribution setup, five 20% high-purity-germanium (HPGe) detectors were placed at $\theta_{\text{lab}} = 0°, 45°, 90°, 135°$, and 150° relative to the beam axis. Detectors 1 through 4 were positioned 8 cm from the target while detector 5 was placed at 12 cm because of limitations in the geometry of the setup, as shown in Fig. 2(a). For the second setup, a HPGe clover detector, consisting of four 25% crystals, was positioned in close proximity to the target at an angle of 45° with respect to

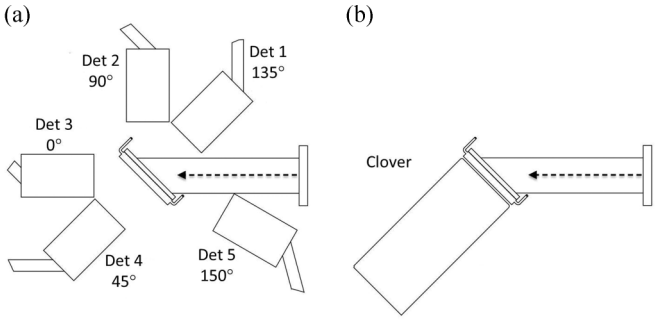

FIG. 2. (a) Detector setups of the angular distribution measurement and (b) of the clover detector.

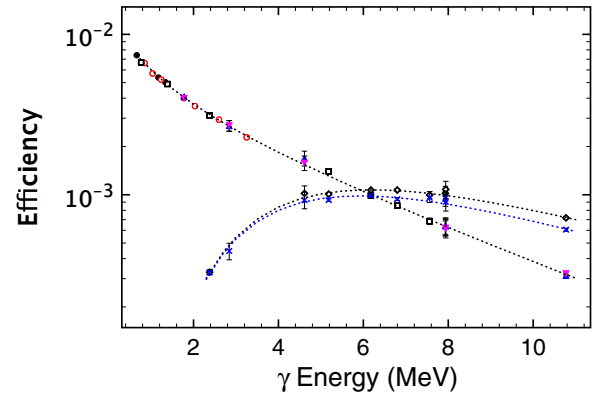

FIG. 3. Peak efficiency for the clover setup at 1 cm. The data shown are summing corrected measurements. The data are ^{137}Cs and ^{60}Co sources (solid circles), ^{56}Co source (open circles), ^{14}N$(p,\gamma)^{15}$O reaction (open squares), ^{27}Al$(p,\gamma)^{28}$Si reaction at 1 cm (up triangles), at 20 cm but scaled to match 1 cm measurements (down triangles), SEP (diamonds), and DEP (crosses) measurements. The dotted lines are fits to the data.

the beam direction, as shown in Fig. 2(b). The distance was increased to 5 cm to reduce coincidence summing effects for higher-energy measurements ($0.8 < E_p < 3.4$ MeV). To test consistency, measurements were made at the same energies using both setups. Lead attenuators (≈3 mm thick) were placed in front of the detectors to reduce the count rate from low-energy background γ radiation when running at higher beam energies. A liquid-nitrogen-cooled copper cold finger biased to −400 V limited carbon build-up and suppressed secondary electrons. The target backing was constantly cooled with recirculating deionized water.

Efficiencies were measured by using ^{56}Co, ^{60}Co, and ^{137}Cs γ-ray sources. To cover the higher γ-ray-energy range, transitions from well-known resonances in the ^{27}Al$(p,\gamma)^{28}$Si ($E_p = 992$ keV [20]) and ^{14}N$(p,\gamma)^{15}$O ($E_p = 278$ keV) reactions were used. The absolute cross sections were determined by normalizing to the strength, $\omega\gamma = 13.1 \pm 0.6$ meV [4], of the $E_p = 278$ keV resonance in the ^{14}N$(p,\gamma)^{15}$O reaction. Single-escape-peak (SEP) and double-escape-peak (DEP) efficiencies were also calculated. A polynomial function of third order was used to fit the full-energy-peak (FEP) efficiency [21]:

$$\epsilon\left(E_\gamma\right) = \exp\left\{\sum_{i=0}^{n} a_i \ln(E)^i\right\}, \tag{1}$$

while for escape-peak efficiencies, only second-order polynomials were necessary. A fit to the efficiency of the clover detector setup is shown in Fig. 3.

The total efficiency, which describes the probability that any amount of energy from an incident γ ray is deposited in the detector, is important for summing corrections. The total efficiency was first calculated by simulating the experimental setup with GEANT4 [22]. The simulated total efficiency curve was then normalized to the measured ^{137}Cs and ^{60}Co total efficiencies. Since ^{137}Cs is a single-line γ-ray emitter, the total efficiency at $E_\gamma = 661$ keV can be directly determined from the measurement. A ^{60}Co source emits γ rays at 1173 and 1332 keV and a sum peak was observed at 2505 keV. The total efficiency of the two γ rays at an average energy of $E_\gamma = 1253$ keV can be calculated by using the sum-peak method [23]:

$$\eta_{\text{total}}(1253\text{ keV}) = \frac{1}{W} - \frac{1}{W}\sqrt{\frac{N_{1173}N_{1332}}{N_{2505}N_t + N_{1173}N_{1332}}}, \tag{2}$$

where W is the angular correlation of the 1173 and 1332 keV γ rays and N_t is the total counts in the spectrum.

Summing corrections are crucial when measuring the γ-ray transitions in the vicinity of the $E_p = 278$ keV resonance with the detector placed in close geometry. The decay scheme of the corresponding compound nucleus state at $E_x = 7.56$ MeV is very simple because all secondary transitions have 100% branching ratios to the ground state. Thus all primary (except for the ground-state transition) and secondary transitions have non-negligible summing-out effects, which can be described by using [21]

$$Y_i^{\text{pri}} = Rb_i\epsilon_{\text{fep}}\left(E_i^{\text{pri}}\right)\left[1 - \epsilon_{\text{tot}}\left(E_i^{\text{sec}}\right)\right], \tag{3}$$

$$Y_i^{\text{sec}} = Rb_i\epsilon_{\text{fep}}\left(E_i^{\text{sec}}\right)\left[1 - \epsilon_{\text{tot}}\left(E_i^{\text{pri}}\right)\right]. \tag{4}$$

Here, Y_i represents the measured yields of the primary or secondary ("pri" or "sec") transition, R is the number of reactions per incoming particle, b_i are the branching ratios, and ϵ_{fep} and ϵ_{tot} are the full energy peak FEP and total efficiency of the corresponding transition, respectively.

For the ground-state transition, the summing-in effect needs to be considered. When a cascade transition through an intermediate level occurs, there is a possibility that the FEPs of both transitions are detected simultaneously. This results in a peak at the same energy as the FEP ground-state transition (summing-in effect), which can be corrected by using

$$Y_{\text{g.s.}} = Rb_{\text{g.s.}}\epsilon_{\text{fep}}(E_{\text{g.s.}}) + R\sum_i b_i\epsilon_{\text{fep}}\left(E_i^{\text{pri}}\right)\epsilon_{\text{fep}}\left(E_i^{\text{sec}}\right). \tag{5}$$

The subscript i denotes the cascade transitions through the energy levels at $E_x = 6.79$, 6.17, and 5.18 MeV. A general approach to the summing correction can be found in Ref. [24]. All measured yields were corrected for summing. The ground-state-transition yield was corrected by using all the cascade transitions that were observed. For setup (b) [Fig. 2(b)] at 1 cm, only data with less than a 5% correction were used. For

the same setup at 5 cm and setup (a) [Fig. 2(a)], the correction is less than 1%.

The experimental angular distribution can be described as

$$W_{\text{expt}}(\theta) = a_0\left(1 + \sum_{i=1}^{n} a_i Q_i P_i(\cos\theta)\right), \tag{6}$$

where a_i are the angular distribution coefficients and Q_i are the attenuation factors due to the finite size of the detector. The $P_i(\cos\theta)$ are the Legendre polynomials of order i. The Q_i, which are geometric correction factors for the finite solid angle subtended by the detector, are given by [25]

$$Q_i = \frac{\int_0^{\beta_{\max}} P_i(\cos\beta)\eta(\beta,E)\sin\beta d\beta}{\int_0^{\beta_{\max}} \eta(\beta,E)\sin\beta d\beta}, \tag{7}$$

where β is the angle between the incident γ ray on the detector and the detector symmetry axis, and $\eta(\beta,E)$ is the detector efficiency at energy E_γ and angle β.

The Q_2 coefficient was measured by using the DC $\rightarrow$ 0.50 MeV γ-ray transition of the $^{16}\text{O}(p,\gamma)^{17}\text{F}$ reaction at $E_p = 0.805$ MeV. This transition is dominated by $E1$ direct capture [26]. The angular distribution of the direct-capture transition depends only on the initial and final orbital angular momenta. The 0.50 MeV state has a spin-parity of $1/2^+$ ($l_f = 0$), thus a p-wave-capture process will produce $E1$ capture. The angular distribution of such a process is given by [26]

$$W(\theta) = 1 - P_2(\cos\theta). \tag{8}$$

Experimentally, $W_{\text{expt}}(\theta) = a_0[1 - Q_2 P_2(\cos\theta)]$. The fits to the measured yield are shown in Fig. 4. The measured values are $Q_2 = 0.92 \pm 0.05$ for setup (a) at 8 cm and 0.78 ± 0.02 for setup (b) at 5 cm. The angular dependence is consistent with the GEANT4 simulations [27]. The GEANT4 simulations are then scaled according to the measured Q_2 values in order to determine the other coefficients. All coefficients used in the calculations are summarized in Table I.

TABLE I. Angular attenuation coefficients used for solid angle corrections.

Detector setup	Q_1	Q_2	Q_3	Q_4
Clover Ge 1 cm	0.73(1)	0.38(2)	0.07(5)	−0.10(10)
Clover Ge 5 cm	0.95(1)	0.78(2)	0.56(4)	0.34(7)
Single Ge 8 cm	0.95(3)	0.92(5)	0.89(10)	0.84(16)

III. ANALYSIS

The angle-integrated cross sections of both the ground state and the $E_x = 6.79$ MeV transitions are calculated by fitting Legendre polynomials to the differential data. It should be emphasized that the angle-integrated cross sections that were determined in this way are only used for comparison with previous analyses. The R-matrix analysis was performed directly with the differential-cross-section data. The analysis is detailed in the following sections.

A. Angle-integrated cross section and angular distribution coefficients

The angle integrated cross section and the angular distribution coefficients for both transitions were obtained by fitting Legendre polynomials to the data as given in Eq. (6) to second order. The angle-integrated cross-section data are plotted together with that of Imbriani [11], Runkle [12], and the summing-in corrected Schröder data [4] in Figs. 5 and 6. It can be seen that there are significant differences between the angle-integrated data obtained from this work and that of Ref. [9]. The source of these discrepancies is unclear but the difference in the $E_x = 6.79$ MeV transition, in particular the larger values of the cross-section data of Ref. [9] at $E_{\text{c.m.}} > 1.2$ MeV, is discussed further in Sec. III B where it is compared with the external-capture-model calculations.

The angular distribution coefficients in Eq. (6) for the $E_x = 6.79$ MeV primary transition are plotted in Fig. 7 and are compared with those of Schröder *et al.* [9] where only an a_2 term was considered. The a_1 coefficient is measured to be

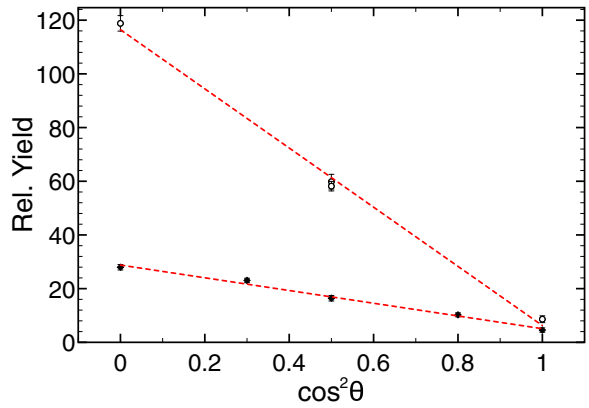

FIG. 4. Q_2 measurements using the $^{16}\text{O}(p,\gamma_{0.50})^{17}\text{F}$ reaction. The dotted lines are fits to the data using $Y = a_0\{1 - Q_2 P_2[\cos(\theta)]\}$. The relative yields from two different setups are scaled to be better presented in one plot. The measurements are the clover setup at 5 cm (diamonds) and the angular distribution setup (circles).

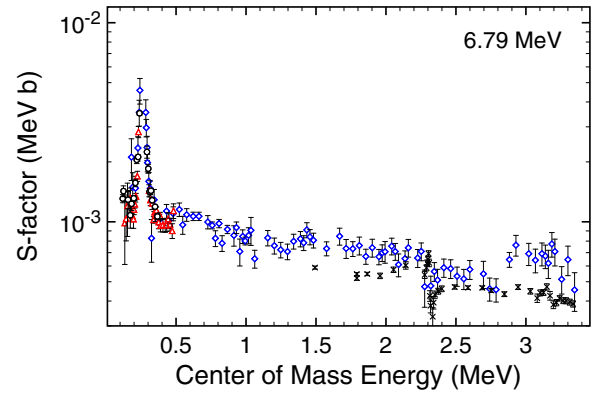

FIG. 5. S factor of the $E_x = 6.79$ MeV primary transition. The data shown are from Ref. [9] (diamonds), Ref. [12] (triangles), Ref. [11] (circles), and the present measurement (crosses). Note that the statistical uncertainties on several of the present measurements are smaller than the symbols.

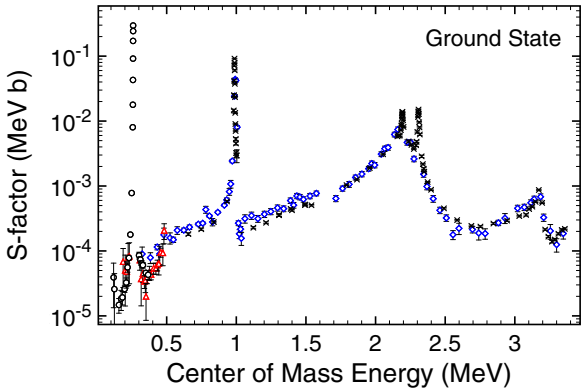

FIG. 6. S factor of the ground-state transition. The data shown are from Ref. [9] (diamonds), Ref. [12] (triangles), Ref. [11] (circles), and the present measurement (crosses). Note that the statistical uncertainties on several of the present measurements are smaller than the symbols.

≈0.1–0.2 with a slightly increasing slope and the a_2 coefficient is -1. The spin-parity of the $E_x = 6.79$ MeV state is $3/2^+$ ($l_f = 0$) and this transition is dominated by the direct capture process. If it is assumed that the $E1$ component dominates the direct capture, the angular distribution of this transition should be $W(\theta) = \sin^2\theta$ [26], which results in $a_1 = 0$ and $a_2 = -1$. The statistically significant deviation of the a_1 coefficient from 0 indicates the presence of another component to the reaction, which is discussed in Sec. III B.

Both the a_1 and the a_2 coefficients of the ground-state transition are dominated by resonant captures over the entire region. It is therefore difficult to isolate the direct component of the angular distribution. To illustrate the direct capture contribution, the solid blue lines in Fig. 8 represent the R-matrix calculation of the external-capture contribution.

B. Multichannel R-matrix analysis

An R-matrix analysis [28,29] using the code AZURE2 [16] was used to simultaneously fit all the ground state and the $E_x = 6.79$ MeV primary transition differential-cross-section data measured in the current experiment. Only statistical uncertainties were included in the fitting. Since the normalization of the external capture component is determined by its corresponding asymptotic normalization coefficient (ANC) [30], the fits to the two transitions were made simultaneously so that the ANC of the $E_x = 6.79$ MeV bound state could be directly constrained by the data from both. This then provides significantly greater constraint and ensures consistency between the ground-state subthreshold contribution and the direct capture to the $E_x = 6.79$ MeV transition. The channel radius was fixed at 5.5 fm, which was adopted from Ref. [11]. Variations from this value and their influence on the extrapolation of the cross section are discussed in Sec. III C. All the proton ANCs were fixed to the recommend values in Refs. [4,16] except for the $E_x = 6.79$ MeV state which was allowed to vary as a free parameter. The starting values of level energies and widths were adopted from Ref. [19] but allowed to vary in the fit.

For the $E_x = 6.79$ MeV transition, radiative capture dominates the cross section and is reproduced very well by a pure-external-capture model [16,31], with no background state necessary. Usually, it is assumed that only the $E1$ component is important. But $E1$ alone is not sufficient to describe the asymmetry observed between the 45° and 135° differential-cross-section data. With only the $E1$ component, the ratio between the yields of these two angles should be equal to 1, but the data clearly deviate, as shown in Fig. 9. By including the $E2$ component and the corresponding $E1/E2$ interference, the experimental data are reproduced at all angles and energies (Fig. 10). This is in contrast to previous R-matrix analyses of the data of Ref. [9]. Because these data have a larger cross section than that produced by a pure-external-capture calculation at $E_{\text{c.m.}} > 1.2$ MeV, external-capture calculations had been combined with a background pole contribution to reproduce the data [4]. The more accurate data of this work show this background contribution to be unnecessary. It should be noted that, at higher energies, $E_{\text{c.m.}} > 2.8$ MeV, pure external capture fails to reproduce the cross section over some small energy regions. These discrepancies are attributed to weak resonance contributions from several levels at these higher energies [19] that are not included in the R-matrix calculations.

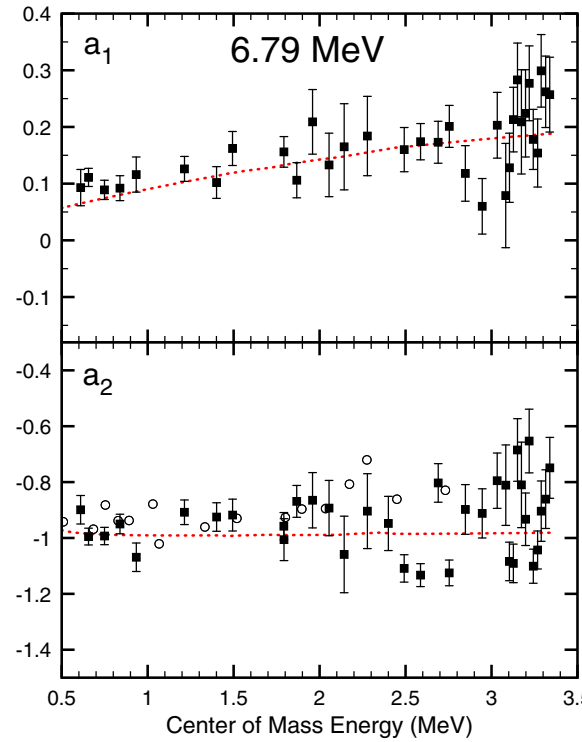

FIG. 7. The a_1 and a_2 coefficients of the $E_x = 6.79$ MeV primary transition. The data shown are the present data (squares) from Legendre polynomial fits and those of Ref. [9] (circles) where only the a_2 term was considered. The dotted lines represent calculations from an R-matrix fit. Note that the a_2 coefficients from the R-matrix fit are systematically lower than both measurements but are in significantly better agreement with those of the current measurement. The reason for the large disagreement between the R-matrix fit and the data of Ref. [9] is unknown. Sometimes, the present experimental values are above the R-matrix predictions because there are weak resonance transitions over this energy region that have not been included.

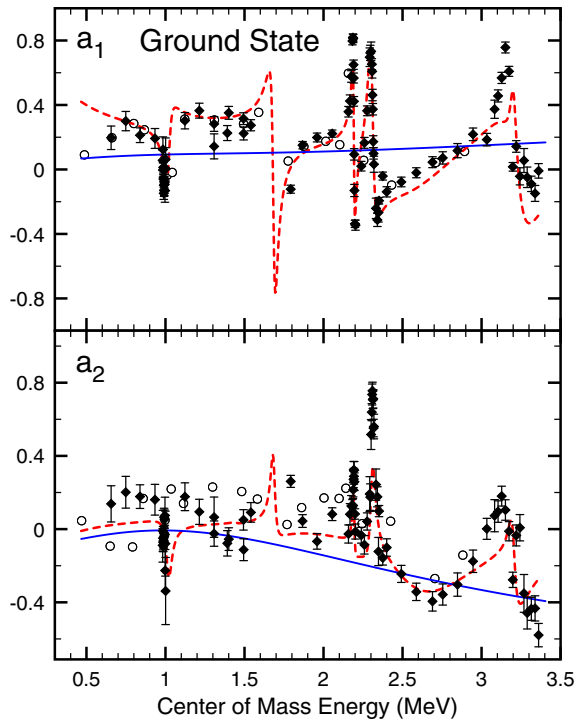

FIG. 8. The a_1 and a_2 coefficients resulting from the angular analysis of the ground-state transition. The data shown are from Ref. [9] (circles) and polynomial fits of the present data (diamonds). The dashed lines represent calculations from an R-matrix fit. The blue solid lines represent external-capture calculations based on the R-matrix fit.

The fitted ANC for the $E_x = 6.79$ MeV state is $C_{s3/2} = 4.91 \pm 0.07(\text{stat}) \pm 0.17(\text{syst})\ \text{fm}^{-1/2}$, which is in good agreement with values from transfer experiments of 4.6(5) [32] and 5.2(6) [30], but somewhat larger than the range of values 4.61(2), 4.65(2), and 4.69(2) $\text{fm}^{-1/2}$ (for radii of 4.14, 4.6, and 5.4 fm, respectively) obtained by the R-matrix fits (angular momentum $l = 0$ only) of Ref. [4].

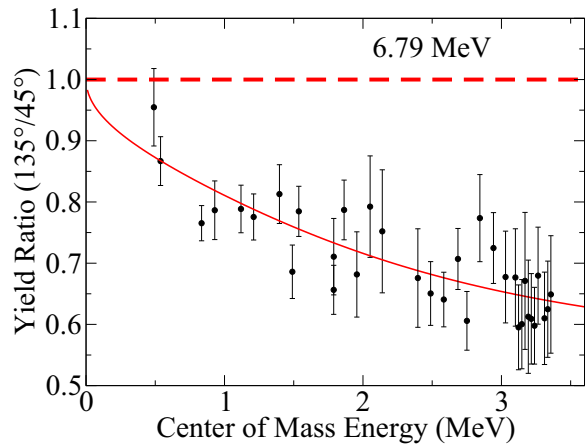

FIG. 9. Ratio between the $E_x = 6.79$ MeV transition yield measured at $\theta_{\text{lab}} = 45°$ and 135°. The dotted line represents the ratio if only $E1$ external capture is included. The solid line represents the inclusion of $E1$ and $E2$ external capture and the interference between them. The data in the vicinity of the narrow resonances have been excluded.

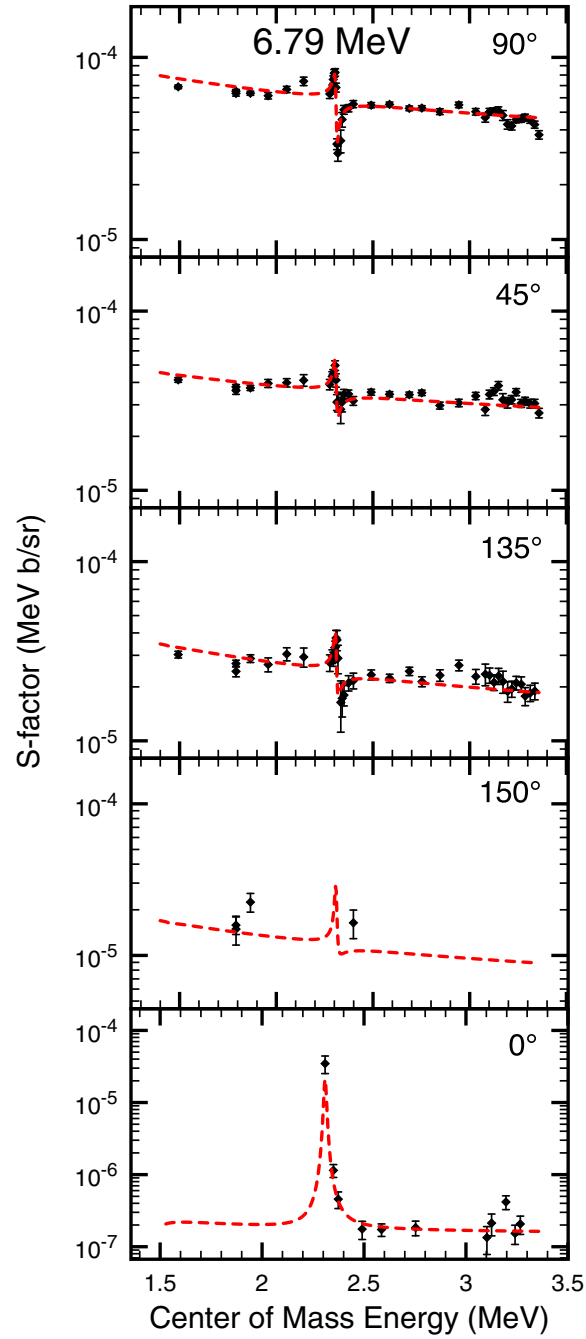

FIG. 10. R-matrix fit to the differential S factors of the $E_x = 6.79$ MeV primary transition. The resonance at $E_R = 2.31$ MeV was included in the fit but does not contribute significantly to the low-energy S factor.

The ground-state transition shows a more complicated structure. Angular momenta of $l_i = 2$ were included in the cross-section calculations for the resonant contributions from the $E_x = 8.28$ and 9.48 MeV $3/2^+$ levels since the differential-cross-section data cannot be reproduced with only $l_i = 0$ channels. To mimic the contribution from higher energy levels, a $3/2^+$ background pole at $E_x = 15$ MeV was also included in

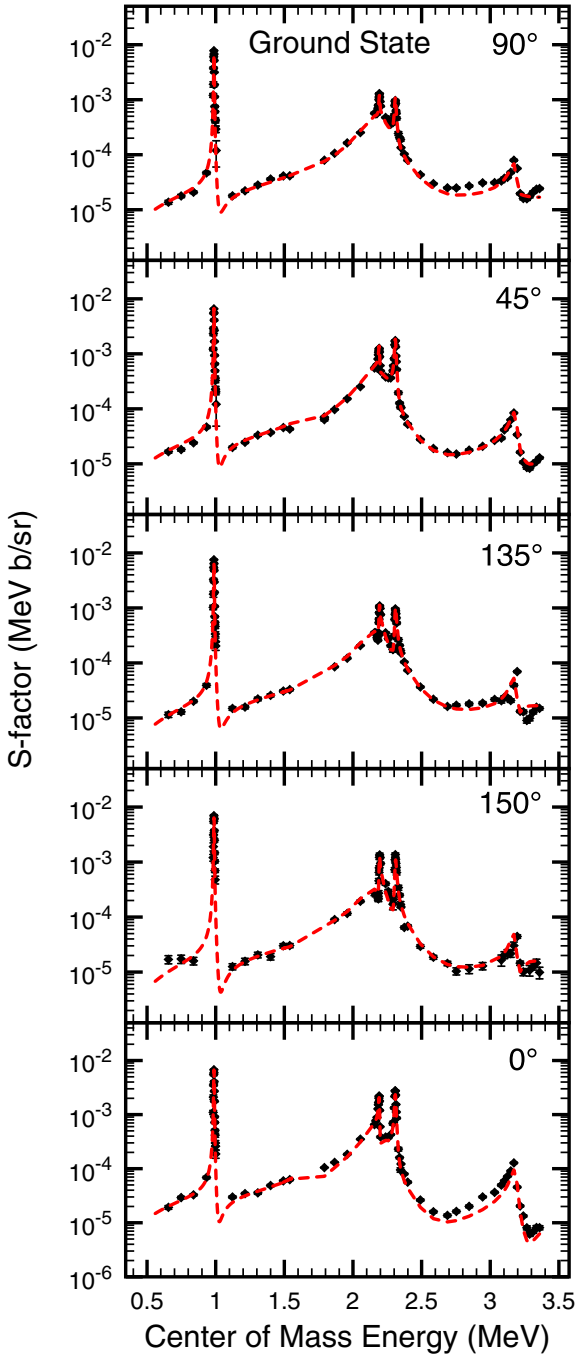

FIG. 11. R-matrix fit to the differential S factors from the ground-state transition.

the fit. Other background pole contributions were also tested but only that of the $3/2^+$ was found to be necessary. Furthermore, only the $l_i = 0$ channel of the $3/2^+$ background pole was found to have a significant effect on the fit. To fit the resonance at $E_R = 3.2$ MeV ($E_x \simeq 10.5$ MeV), decay contributions from two levels at $E_x = 10.48$ MeV and 10.51 MeV [19] were necessary. The starting values for the energies and widths were taken from Ref. [19] and were allowed to vary during the fit. Since the spin-parities of both levels are not determined in the literature, different combinations of up to a spin of $5/2$ were tested for these two states. The best fit was achieved with

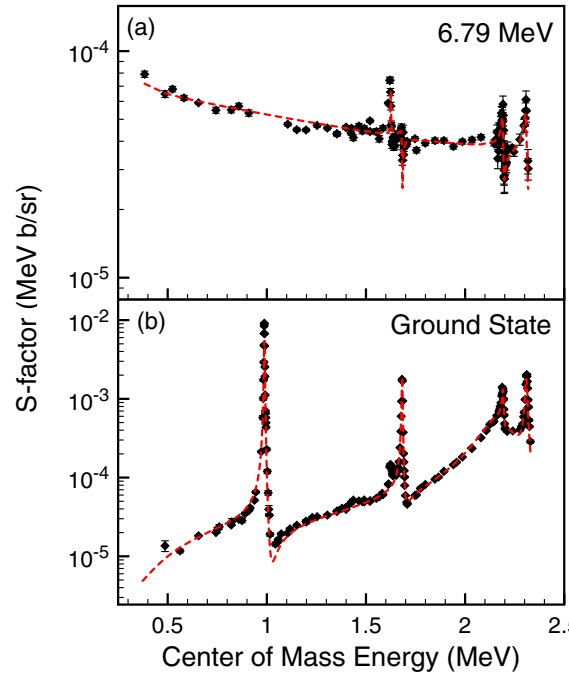

FIG. 12. R-matrix fit to the differential S factors obtained by using the clover detector setup at $\theta_{\rm lab} = 45°$. The transition to the state at $E_x = 6.79$ MeV and the ground-state transition are shown in panels (a) and (b), respectively.

spin-parity assignments of either $3/2^-$ or $3/2^+$, as shown in Fig. 11. The fit to the differential-cross-section data measured with the clover setup [Fig. 2(b)] are plotted in Fig. 12. All parameters used in the fits are summarized in Table II.

It should be questioned if this large background pole contribution is actually physically reasonable. The data of Ref. [33] cover a wider higher energy range from $E_p = 2.2$ to 19 MeV. These data display several broad resonances, interpreted as a fractured giant dipole resonance, with total widths estimated at $\sim$1 MeV and often larger. These data lie at energies where several other particle channels open so a complete fitting has not been achieved, but preliminary calculations can be made by assuming that the ground-state proton channel dominates. By normalizing the data of Ref. [33] to the present data in the overlapping energy range ($E_p = 2.2$ to 3.6 MeV), the γ_0 widths of the broad states at $E_x \approx 12.95$ ($\Gamma_p \approx 250$ keV, $\Gamma_{\gamma_0} \approx 7$ eV) and $E_x \approx 13.9$ MeV ($\Gamma_p \approx 3$ MeV, $\Gamma_{\gamma_0} \approx 160$ eV) were estimated. Assuming these states are $J^\pi = 3/2^+$ (Refs. [33] indicates tentative spins assignments of either $1/2^+$ or $3/2^+$), the low-energy tails of just these two levels leads to a low-energy contribution very similar to the background pole contribution deduced from the present data. Therefore, the higher-energy data are in support of such a background component.

C. The zero energy S factor for the $E_x = 6.79$ MeV and ground-state transitions

The extrapolations of S factors to zero energy for both transitions were calculated from the R-matrix fit. The results are summarized in Table III together with previous literature

TABLE II. Parameters used in the R-matrix fit. Bold values are fixed during the fit. The signs on the partial widths and ANCs indicate the relative interferences. The dividing line demarcates the proton separation energy at $E_x = 7.2968(5)$ MeV [19]. The quoted uncertainties from this work are statistical only.

E_x (Ref. [19])	E_x (fit)	J^π	Channel	l	s	$\frac{\text{ANC (fm}^{-1/2})}{\text{Partial width (eV)}}$
0.0	**0**	$1/2^-$	$^{14}\text{N}+p$	1	1/2	**0.23**
			$^{14}\text{N}+p$	1	3/2	**7.4**
5.183(1)	**5.183**	$1/2^+$	$^{14}\text{N}+p$	0	1/2	**0.33**
			$^{15}\text{O}+\gamma_{0.00}$	$E1$	1/2	**0.0784**
5.2409(3)	**5.2409**	$5/2^+$	$^{14}\text{N}+p$	2	1/2	**0.23**
			$^{14}\text{N}+p$	2	3/2	**0.24**
			$^{15}\text{O}+\gamma_{0.00}$	$M2$	1/2	**0.0002**
6.1763(17)	**6.1763**	$3/2^-$	$^{14}\text{N}+p$	1	1/2	**0.47**
			$^{14}\text{N}+p$	1	3/2	**0.53**
			$^{15}\text{O}+\gamma_{0.00}$	$M1$	1/2	**0.875**
6.7931(17)	**6.7931**	$3/2^+$	$^{14}\text{N}+p$	0	3/2	4.91(7)
			$^{15}\text{O}+\gamma_{0.00}$	$E1$	1/2	2.7(2)
6.8594(9)	**6.8594**	$5/2^+$	$^{14}\text{N}+p$	2	1/2	**0.39**
			$^{14}\text{N}+p$	2	3/2	**0.42**
7.2759(6)	**7.2759**	$7/2^+$	$^{14}\text{N}+p$	2	3/2	**1541**
7.5565(4)	**7.5565**	$1/2^+$	$^{14}\text{N}+p$	0	1/2	$\mathbf{0.96\times10^{3}}$
			$^{15}\text{O}+\gamma_{0.00}$	$E1$	1/2	$\mathbf{0.65\times10^{-3}}$
			$^{15}\text{O}+\gamma_{6.79}$	$M1$	3/2	$\mathbf{9.3\times10^{-3}}$
8.2840(5)	8.28514(4)	$3/2^+$	$^{14}\text{N}+p$	2	1/2	$-0.11(3)\times10^{3}$
			$^{14}\text{N}+p$	0	3/2	$3.64(4)\times10^{3}$
			$^{14}\text{N}+p$	2	3/2	$-0.38(3)\times10^{3}$
			$^{15}\text{O}+\gamma_{0.00}$	$E1$	1/2	0.22(1)
8.743(6)	8.7491(3)	$1/2^+$	$^{14}\text{N}+p$	0	1/2	$36.7(8)\times10^{3}$
8.922(2)	8.92104(4)	$5/2^+$	$^{14}\text{N}+p$	2	3/2	$3.86(6)\times10^{3}$
			$^{15}\text{O}+\gamma_{6.79}$	$M1$	3/2	$3.2(3)\times10^{-3}$
8.9821(17)	8.97996(2)	$5/2^-$	$^{14}\text{N}+p$	1	3/2	$-5.69(5)\times10^{3}$
			$^{15}\text{O}+\gamma_{0.00}$	$E2$	1/2	$-0.29(1)$
			$^{15}\text{O}+\gamma_{6.79}$	$E1$	3/2	$3.7(2)\times10^{-3}$
9.484(8)	9.5024(7)	$3/2^+$	$^{14}\text{N}+p$	2	1/2	$89(2)\times10^{3}$
			$^{14}\text{N}+p$	0	3/2	$125(8)\times10^{3}$
			$^{15}\text{O}+\gamma_{0.00}$	$E1$	1/2	7.4(3)
9.488(3)	9.48938(7)	$5/2^-$	$^{14}\text{N}+p$	3	1/2	$0.85(5)\times10^{3}$
			$^{14}\text{N}+p$	1	3/2	$-7.3(3)\times10^{3}$
			$^{14}\text{N+p}$	3	3/2	$-1.1(2)\times10^{3}$
			$^{15}\text{O}+\gamma_{0.00}$	$E2$	1/2	$-0.34(2)$
			$^{15}\text{O}+\gamma_{6.79}$	$E1$	3/2	0.013(2)
9.609(2)	9.6060(1)	$3/2^-$	$^{14}\text{N}+p$	1	3/2	$-13.0(3)\times10^{3}$
			$^{15}\text{O}+\gamma_{0.00}$	$M1$	1/2	1.25(6)
			$^{15}\text{O}+\gamma_{6.79}$	$E1$	3/2	$-0.034(3)$
10.480	10.497(2)	$3/2^-$	$^{14}\text{N}+p$	1	1/2	$104(7)\times10^{3}$
			$^{14}\text{N}+p$	1	3/2	$-26(2)\times10^{3}$
			$^{15}\text{O}+\gamma_{0.00}$	$M1$	1/2	0.31(3)
10.506	10.478(6)	$3/2^+$	$^{14}\text{N}+p$	2	1/2	$-2.4(20)\times10^{3}$
			$^{14}\text{N}+p$	0	3/2	$40(2)\times10^{3}$
			$^{14}\text{N}+p$	2	3/2	$7(1)\times10^{3}$
			$^{15}\text{O}+\gamma_{0.00}$	$E1$	1/2	0.38(2)
	15	$3/2^+$	$^{14}\text{N}+p$	0	3/2	$8.9(5)\times10^{6}$
			$^{15}\text{O}+\gamma_{0.00}$	$E1$	1/2	220(20)

values. The $S_{6.79}(0)$ is in very good agreement with Ref. [16] but about 10% higher than the value from case (ii) in Ref. [4], as shown in Fig. 13. External-capture fits have had difficulty reproducing the high-energy portion of the $E_x = 6.79$ MeV transition data of Ref. [9], as discussed in Refs. [4,10]. The present measurements and analysis have revealed this to be a twofold issue. The first can be seen by a comparison between the angle-integrated data deduced in the present work with that of Ref. [9], as shown in Fig. 5. There is a clear difference in the energy dependence of the data from this work with that of

TABLE III. Summary of $S(0)$ values. Systematic uncertainties dominate both transitions' uncertainty budgets.

Ref.	$S_{\text{g.s.}}(0)$ (keV b)	$S_{6.79}(0)$ (keV b)
Imbriani *et al.* [11]	0.25 ± 0.06(syst)	1.20 ± 0.05(syst)
Runkle *et al.* [12]	0.49 ± 0.08(stat) ± 0.05(syst)	1.15 ± 0.05(stat) ± 0.11(syst)
Azuma *et al.* [16]	0.28	1.30
Adelberger *et al.* [4]	0.27 ± 0.05(syst)	1.18 ± 0.08(syst)
Present	0.42 ± 0.04(stat)$^{+0.09}_{-0.19}$(syst)	1.29 ± 0.04(stat) ± 0.09(syst)

Ref. [9], where the data of Ref. [9] exhibit larger cross sections over several energy regions. The second issue, although much less significant, is the inclusion of the $E2$ multipolarity in the external-capture cross section. While this is quite important for the differential data because of the interference between the $E1$ and $E2$ external-capture components, the effect is greatly reduced in the angle-integrated data. While the $E2$ contribution increases relative to the $E1$ contribution at higher energies, even for the highest-energy data points at $E_{\text{c.m.}} = 3.3$ MeV, the $E2$ external capture is at most only about 3% of the $E1$ contribution.

The predicted $S_{\text{g.s.}}(0) = 0.42 \pm 0.04(\text{stat})^{+0.09}_{-0.19}$ (syst) keVb, based on the fit to only the data from the present work, is larger than previous extrapolations except for that of Runkle [12], as shown in Figs. 14 and 15. The dashed green line in Fig. 14 has been taken from Ref. [16] where $l_i = 2$ has been included. This fit gives an increase in the value of $S_{\text{g.s.}}(0)$ although it was not included in their final values. The discrepancies are even larger at energies near the lower-energy side of the $E_p = 278$ keV resonance.

The interpretation of the higher-energy ground-state transition data is complicated by several resonances, a strong subthreshold state contribution from the $E_x = 6.79$ MeV state, direct capture to the ground state, and multiple possible angular momentum or channel spin l-s entrance channels in the R matrix. Furthermore, a strong $3/2^+$ background state also seems necessary to fit the data [10,16]. This analysis, as well as previous works, show that $S_{\text{g.s.}}(0)$ is very sensitive to the γ width of the $E_x = 6.79$ MeV subthreshold state. Contributions from other subthreshold states were also investigated, but their contributions were found to be negligible. The value of the ground state width from the fit is $\Gamma_\gamma(6.79) = 2.7 \pm 0.2$(stat) eV and is in agreement with the lower-limit lifetime measurement by Ref. [34] of >0.85 eV but is considerably larger than the values of 0.41^{+34}_{-13} eV (90% C.L.) of Ref. [35] and $0.95^{+0.60}_{-0.95}$ eV of Ref. [36].

The low-energy data of Refs. [11,12,15] are not included in the fit, but a comparison of the data to the present fit is shown in Fig. 14. The calculation overestimates the low-energy data by a significant amount. This deviation of the R-matrix fit from the data is exactly the same as that encountered by Ref. [16] when higher-order entrance channel angular momenta ($l \geqslant 2$) were included in their fit, as they show in Fig. 8 of that work. Numerous calculations were performed in order to try to resolve this issue on the R-matrix side, including variations of the overall normalizations of the data sets, fixing the ground-state γ width of the $E_x = 6.79$ MeV resonance at different values, allowing the ground-state ANC to vary freely, including other background poles up to $J = 5/2$, and trying multiple background poles at different energies. None of these were found to alleviate the issue. The fit is very sensitive to

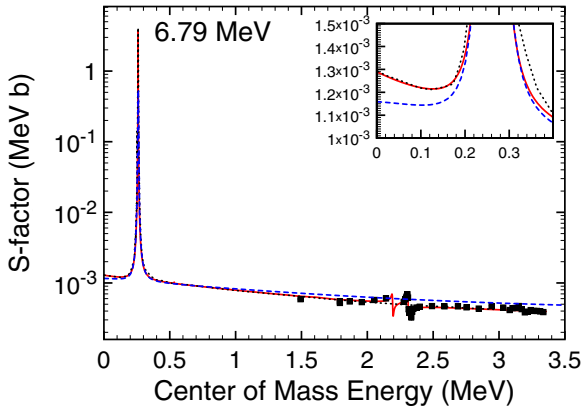

FIG. 13. R-matrix calculation of the $E_x = 6.79$ MeV S factor using the parameters from the R-matrix fit (solid) together with the R-matrix fit from Ref. [16] (dotted), and case (ii) from Ref. [4] where the data sets were limited to $E_{\text{c.m.}} < 1.2$ MeV (dashed). The data are those from the angular distribution measurements of the present work that were fit with Eq. (6) to obtain angle-integrated cross sections that have then been transformed to S factors. The inset shows the extrapolation to zero energy.

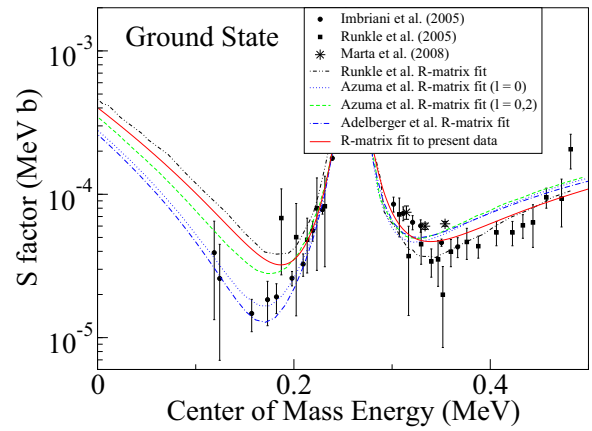

FIG. 14. Extrapolation of the R-matrix fit to the higher-energy data of this work (red solid line). The fit is compared to the low-energy data of Refs. [11,12,15] and previous R-matrix extrapolations from Refs. [4,12,16]. The large inconsistencies between both the different data sets and the R-matrix extrapolations leads to a large systematic uncertainty in the value of $S(0)$ for the ground-state transition.

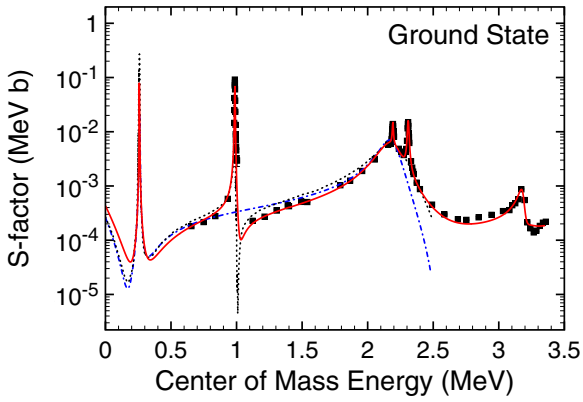

FIG. 15. R-matrix calculation of the ground-state S factor using the parameters from the best fit (solid) together with the fit from Ref. [16] (dotted) and Ref. [4] (dash-dot).

the value of the ground-state γ width of the subthreshold state and one issue is that there is a strong disagreement between the favored value of the low-energy data of Ref. [11] and the present higher-energy data. The present data favor a larger value of $\Gamma_{\gamma_0}^{6.79} = 2.7(2)$ eV while the data of Ref. [11] favor a smaller value of 0.8(4) eV.

To investigate the uncertainty range and the contributions of the different reaction components to the overall uncertainty, a Monte Carlo uncertainty analysis, similar to that described in Ref. [37], has been performed on the present data. Variations in the channel radius were also investigated and the results of Refs. [11,12] were reaffirmed. That is, over a range from 5 to 6.5 fm a change in channel radius resulted in a change in $S(0)$ of <5%. For the transition to the $E_x = 6.79$ MeV state, the statistical contribution to the uncertainty in the zero-energy S factor was found to considerably smaller than that quoted by Ref. [4]. This was a result of the smaller statistical uncertainties than the previous higher-energy data of Ref. [9] and the assertion that the $E_x = 6.79$ MeV cross section can be described purely by external capture (that is, no background pole contribution is necessary to describe the data). For the ground-state transition, the statistical contribution is found to be ≈10%. Furthermore, there are significant inconsistencies in both low-energy ground-state data and the R-matrix fits. Therefore a systematic uncertainty in the ground-state transition covering the range between that determined by Ref. [11] [$S(0) = 0.25$ keV b] and that of Ref. [12] [$S(0) = 0.49$ keV b] is recommended (similar to the recommendation of Ref. [4]). In addition, there is an overall 7% systematic uncertainty. This results from the normalization to the $E_p = 278$ keV resonance (4.6%), the charge collection (2%), and the efficiency determination and summing corrections (5%).

IV. SUMMARY

The excitation function of the $^{14}\mathrm{N}(p,\gamma)^{15}\mathrm{O}$ reaction has been measured with a clover detector from $E_p = 0.4$ to 2.5 MeV for the ground-state and 6.79 MeV transitions. Angular distributions have also been measured from $E_p = 0.5$ to 3.6 MeV for the ground-state transition and from $E_p = 1.6$ to 3.6 MeV for the $E_x = 6.79$ MeV transition. Both measurements have been made with significantly improved statistical uncertainties and more accurate summing corrections than the previous measurement that covered a similar energy range [9].

A multichannel R-matrix analysis was performed simultaneously for both the ground state and $E_x = 6.79$ MeV transitions. The transitions are closely linked because the $E_x = 6.79$ MeV acts as a subthreshold state in the ground-state transition. The $E2$ external-capture component was found to be crucial in describing the differential-cross-section data of the $E_x = 6.79$ MeV transition and the data are now well described by external capture alone, solving a longstanding discrepancy.

For the ground-state-transition fit, the simultaneous fitting of both transitions acts to directly constrain the ANC of the $E_x = 6.79$ MeV subthreshold state, but the ground-state γ-ray width of the transition to the $E_x = 6.79$ MeV state remains poorly constrained, resulting in a large uncertainty in the low-energy cross section. Additionally, as encountered in Ref. [16], it is reaffirmed that higher-order angular momenta ($l > 0$) are necessary in order to fit the higher-energy data. The inconsistencies between the low-energy data and the extrapolation from higher-energy data result in a large systematic uncertainty in $S(0)$. Additional measurements of the low-energy ground-state transition and the γ_0 width of the $E_x = 6.79$ MeV state are critically needed to further reduce the uncertainty of the total cross section at stellar energies.

ACKNOWLEDGMENTS

Figure 1 was created by using the SciDraw scientific figure preparation system [38]. This research was supported in part by the Notre Dame Center for Research Computing and was funded by the National Science Foundation through Grant No. PHY-1068192 and by the Joint Institute for Nuclear Astrophysics Grant No. PHY08-22648.

[1] M. Wiescher, J. Görres, E. Uberseder, G. Imbriani, and M. Pignatari, Annu. Rev. Nucl. Part. Sci. **60**, 381 (2010).

[2] E. G. Adelberger, S. M. Austin, J. N. Bahcall, A. B. Balantekin, G. Bogaert, L. S. Brown, L. Buchmann, F. E. Cecil, A. E. Champagne, L. de Braeckeleer *et al.*, Rev. Mod. Phys. **70**, 1265 (1998).

[3] G. Imbriani, H. Costantini, A. Formicola, D. Bemmerer, R. Bonetti, C. Broggini, P. Corvisiero, J. Cruz, Zs. Fülöp, G. Gervino *et al.*, Astron. Astrophys. **420**, 625 (2004).

[4] E. G. Adelberger, A. García, R. G. H. Robertson, K. A. Snover, A. B. Balantekin, K. Heeger, M. J. Ramsey-Musolf, D. Bemmerer, A. Junghans, C. A. Bertulani *et al.*, Rev. Mod. Phys. **83**, 195 (2011).

[5] J. N. Bahcall and M. H. Pinsonneault, Phys. Rev. Lett. **92**, 121301 (2004).

[6] A. Serenelli, C. Peña-Garay, and W. C. Haxton, Phys. Rev. D **87**, 043001 (2013).
[7] C. Angulo, M. Arnould, M. Rayet, P. Descouvemont, D. Baye, C. Leclercq-Willain, A. Coc, S. Barhoumi, P. Aguer, C. Rolfs *et al.*, Nucl. Phys. A **656**, 3 (1999).
[8] Y. Xu, K. Takahashi, S. Goriely, M. Arnould, M. Ohta, and H. Utsunomiya, Nucl. Phys. A **918**, 61 (2013).
[9] U. Schröder, H. Becker, G. Bogaert, J. Görres, C. Rolfs, H. Trautvetter, R. Azuma, C. Campbell, J. King, and J. Vise, Nucl. Phys. A **467**, 240 (1987).
[10] C. Angulo and P. Descouvemont, Nucl. Phys. A **690**, 755 (2001).
[11] G. Imbriani, H. Costantini, A. Formicola, A. Vomiero, C. Angulo, D. Bemmerer, R. Bonetti, C. Broggini, F. Confortola, P. Corvisiero *et al.*, Eur. Phys. J. A **25**, 455 (2005).
[12] R. C. Runkle, A. E. Champagne, C. Angulo, C. Fox, C. Iliadis, R. Longland, and J. Pollanen, Phys. Rev. Lett. **94**, 082503 (2005).
[13] A. Lemut, D. Bemmerer, F. Confortola, R. Bonetti, C. Broggini, P. Corvisiero, H. Costantini, J. Cruz, A. Formicola, Zs. Fülöp *et al.*, Phys. Lett. B **634**, 483 (2006).
[14] D. Bemmerer, F. Confortola, A. Lemut, R. Bonetti, C. Broggini, P. Corvisiero, H. Costantini, J. Cruz, A. Formicola, Zs. Fülöp *et al.*, Nucl. Phys. A **779**, 297 (2006).
[15] M. Marta, A. Formicola, G. Gyürky, D. Bemmerer, C. Broggini, A. Caciolli, P. Corvisiero, H. Costantini, Z. Elekes, Zs. Fülöp *et al.* (LUNA Collaboration), Phys. Rev. C **78**, 022802 (2008).
[16] R. E. Azuma, E. Uberseder, E. C. Simpson, C. R. Brune, H. Costantini, R. J. de Boer, J. Görres, M. Heil, P. J. LeBlanc, C. Ugalde *et al.*, Phys. Rev. C **81**, 045805 (2010).
[17] C. Angulo, A. Champagne, and H.-P. Trautvetter, Nucl. Phys. A **758**, 391 (2005).
[18] J. D. Cockcroft and E. T. S. Walton, Proc. R. Soc. London, Ser. A **136**, 619 (1932).
[19] F. Ajzenberg-Selove, Nucl. Phys. A **523**, 1 (1991).
[20] P. Endt, C. Alderliesten, F. Zijderhand, A. Wolters, and A. V. Hees, Nucl. Phys. A **510**, 209 (1990).
[21] G. F. Knoll, *Radiation Detection and Measurement*, 3rd ed. (John Wiley & Sons, Inc., New York, 2000).
[22] S. Agostinelli, J. Allison, K. Amako, J. Apostolakis, H. Araujo, P. Arce, M. Asai, D. Axen, S. Banerjee, G. Barrand *et al.*, Nucl. Instrum. Methods Phys. Res., Sect. A **506**, 250 (2003).
[23] R. Longland, C. Iliadis, A. Champagne, C. Fox, and J. Newton, Nucl. Instrum. Methods Phys. Res., Sect. A **566**, 452 (2006).
[24] P. D. Felice, P. Angelini, A. Fazio, and R. Biagini, Appl. Radiat. Isot. **52**, 745 (2000).
[25] M. E. Rose, Phys. Rev. **91**, 610 (1953).
[26] C. Rolfs, Nucl. Phys. A **217**, 29 (1973).
[27] A. Kontos, J. Görres, A. Best, M. Couder, R. deBoer, G. Imbriani, Q. Li, D. Robertson, D. Schürmann, E. Stech *et al.*, Phys. Rev. C **86**, 055801 (2012).
[28] A. M. Lane and R. G. Thomas, Rev. Mod. Phys. **30**, 257 (1958).
[29] P. Descouvemont and D. Baye, Rep. Prog. Phys. **73**, 036301 (2010).
[30] A. M. Mukhamedzhanov, P. Bém, B. A. Brown, V. Burjan, C. A. Gagliardi, V. Kroha, J. Novák, F. M. Nunes, Š Piskoř, F. Pirlepesov *et al.*, Phys. Rev. C **67**, 065804 (2003).
[31] F. C. Barker and T. Kajino, Aust. J. Phys. **44**, 369 (1991).
[32] P. F. Bertone, A. E. Champagne, M. Boswell, C. Iliadis, S. E. Hale, V. Y. Hansper, and D. C. Powell, Phys. Rev. C **66**, 055804 (2002).
[33] H. Kuan, M. Hasinoff, W. O'Connell, and S. Hanna, Nucl. Phys. A **151**, 129 (1970).
[34] D. Schürmann, R. Kunz, I. Lingner, C. Rolfs, F. Schümann, F. Strieder, and H.-P. Trautvetter, Phys. Rev. C **77**, 055803 (2008).
[35] P. F. Bertone, A. E. Champagne, D. C. Powell, C. Iliadis, S. E. Hale, and V. Y. Hansper, Phys. Rev. Lett. **87**, 152501 (2001).
[36] K. Yamada, T. Motobayashi, H. Akiyoshi, N. Aoi, Zs. Fülöp, T. Gomi, Y. Higurashi, N. Imai, N. Iwasa, H. Iwasaki *et al.*, Phys. Lett. B **579**, 265 (2004).
[37] R. J. deBoer, J. Görres, K. Smith, E. Uberseder, M. Wiescher, A. Kontos, G. Imbriani, A. Di Leva, and F. Strieder, Phys. Rev. C **90**, 035804 (2014).
[38] M. A. Caprio, Comput. Phys. Commun. **171**, 107 (2005); http://scidraw.nd.edu